Journal of The Electrochemical Society, 2023 **170** 104504

A Kinetic Study on H_2 Reduction of Fe_3O_4 for Long-Duration Energy-Storage-Compatible Solid Oxide Iron Air Batteries

Chaitali Morey, Qiming Tang, Shichen Sun, and Kevin Huang[z]

Department of Mechanical Engineering, University of South Carolina, Columbia, South Carolina 29208, United States of America

Long duration energy storage (LDES) is economically attractive to accelerate widespread renewable energy deployment. But none of the existing energy storage technologies can meet LDES cost requirements. The newly emerged solid oxide iron air battery (SOIAB) with energy-dense solid Fe as an energy storage material is a competitive LDES-suitable technology compared to conventional counterparts. However, the performance of SOIAB is critically limited by the kinetics of Fe_3O_4 reduction (equivalent to charging process) and the understanding of this kinetic bottleneck is significantly lacking in the literature. Here, we report a systematic kinetic study of Fe_3O_4-to-Fe reduction in H_2/H_2O environment, particularly the effect of catalyst (iridium) and supporting oxides (ZrO_2 and $BaZr_{0.4}Ce_{0.4}Y_{0.1}Yb_{0.1}O_3$). With in situ created Fe_3O_4, the degree of reduction is measured by the change of H_2O and H_2 concentrations in the effluent using a mass spectrometer, from which the kinetic rate constant is extracted as a function of inlet H_2 concentration and temperature. We find that kinetics can be nicely described by Johson-Mehl-Avrami (JMA) model. We also discuss the stepwise reduction mechanisms and activation energy for the reduction process.

 [DOI: 10.1149/1945-7111/acfbbc]

Manuscript submitted August 3, 2023; revised manuscript received September 19, 2023. Published October 9, 2023. *This paper is part of the JES Focus Issue on SOFC XVIII: Advances in Solid Oxide Fuel Cell and Electrolysis Cell Technology.*

Cost-effective, large-scale stationary storage systems are crucial for grid stability and the integration of renewable energy sources into the utility market. Long-duration electricity storage (LDES) systems with multi-day or seasonal storage capabilities are particularly advantageous for enabling deeper penetration of low-cost wind and solar power.[1–6] While most commercial electricity storage deployments and research and development efforts have focused on systems with durations of around 10 h at rated power, there is a growing recognition of the need for longer-duration storage solutions.[7,8] Existing technologies like pumped-hydro storage (PHS) can provide storage for up to 10 h but are limited in their ability to leverage the full benefits of LDES. Although widely used, conventional lithium-ion batteries face challenges in scaling up to longer durations due to high costs and safety concerns associated with large-scale agglomerated systems. Redox flow batteries offer scalability and safety advantages, but their low energy density and efficiency have limited their application in LDES scenarios. The lack of viable LDES technologies in the utility market is a significant barrier to achieving resilient grid stability and maximizing the potential of renewable energy.

In recent years, we have been researching a new type of metal-air battery for LDES applications. The battery consists of a solid oxide-ion electrolyte and porous electrodes and operates based on oxide-ion chemistry. In this battery, the chemical energy of oxygen is transported in the form of O^{2-} ions through the oxide ion conductor as an electrolyte. The reversible storage of this oxygen chemical energy occurs in an energy-dense Fe/FeO_x bed integrated within the anode chamber of a reversible solid oxide cell (RSOC).[9–12] During the battery's operation, the oxygen electrode (OE) is open to an unlimited oxygen source, typically air while the hydrogen electrode (HE) is enclosed in a low-cost Fe bed chamber. The RSOC alternates between fuel cell mode during discharge and electrolyzer mode during charge. In the fuel cell mode, the battery generates electricity as the oxygen is transferred via a gas phase H_2/H_2O shuttle and stored within the Fe bed through the Fe-O redox reaction. The unique feature of the SOIAB is its direct access to oxygen in the air, eliminating the need for oxygen storage in the OE and making it well-suited for LDES applications.

From our early work, we have identified two major problems limiting the overall performance of a SOIAB: 1) Fe-bed's sluggish FeO_x-to-Fe reduction kinetics;[13] 2) RSOC's high electrode overpotentials.[9] To address these issues, we have previously shown that the synthesis of nanostructured Fe-bed materials[11] and the addition of catalyst (e.g., Pd) nanoparticles can boost the FeO_x-to-Fe reduction kinetics.[9] However, our effort to further improve RSOC's electrochemical performance has been very limited until very recently we demonstrated that adding Ir into Fe-bed can significantly improve the kinetics of FeO_x reduction.[14]

To understand the slow kinetic issue, we have also previously measured the rate constant of the H_2 reduction process of FeO_x-ZrO_2.[15,16] These kinetic data are very useful for our Multiphysics modeling effort. In addition, we have also demonstrated the benefits of replacing ZrO_2 with a proton containing perovskite $BaZr_{0.4}Ce_{0.4}Y_{0.1}Yb_{0.1}O_3$ (BZC4YYb).[17,18] However, there is a lack of reduction kinetics datasets for Ir-catalyzed FeO_x-ZrO_2 and FeO_x-BZCYYb systems. Therefore, the goal of this study is to acquire this set of kinetic data for comparison with the baseline FeO_x-ZrO_2 and future Multiphysics modeling of the battery. The obtained results also provide fundamental insights into the reduction mechanisms as well as engineering data for other large-scale iron-based redox chemical systems such as chemical looping hydrogen, and "green steel" production.

Experimental Methods

Material synthesis.— *Fe_2O_3-ZrO_2 baseline.*—The starting Fe_2O_3/ZrO_2 composite material was prepared by the co-precipitation method. Briefly, the stoichiometric solutions of $Fe(NO)_3.9H_2O$ (≥99%, Sigma-Aldrich) and $ZrO_2(NO)_2.xH_2O$(≥99%, Alfa Aesar, x = 6) were dissolved in deionized water separately in the mole ratios of 85:15. Then these two solutions were mixed with a cation concentration of 0.1 M in a beaker and polyvinylpyrrolidone (PVP, Sigma-Aldrich) as a surface active agent was added while stirring constantly for 30 min. The mixture solution was then added dropwise to an ammonium carbonate $(NH_4)_2CO_3$ (Sigma Aldrich) solution under constant stirring while maintaining the temperature of the solution to 35 °C. To make sure full precipitation of a cation in the solution, the molar ratio of $(NH_4)_2CO_3$ and Mn+ (M = Zr and Fe) was kept as n $(NH_4)_2CO_3$: nMn^+ = 2.5:1. The resultant brownish precipitation was left for 20 h in the solution with continuous stirring. Finally, the suspension was filtered and washed several times with deionized water followed by overnight drying at 80 °C. To obtain the precursor Fe_2O_3/ZrO_2, the collected precipitate

[z]E-mail: huang46@cec.sc.edu

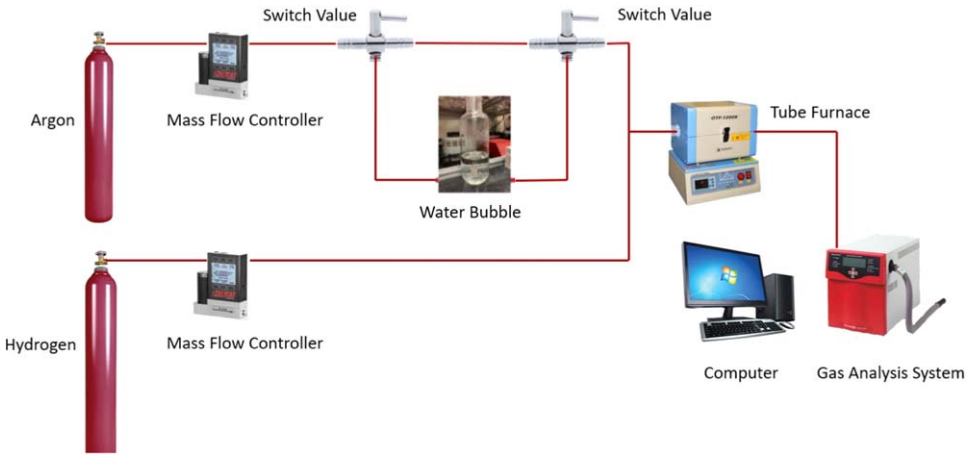

Figure 1. Experimental setup for kinetic study of iron oxide reduction.

was calcined at 600 °C for 5 h. The surface area of the baseline Fe_2O_3/ZrO_2 powder was measured with Micromeritics ASAP2020 surface analyzer.

Fe_2O_3/ZrO_2-Ir.—The prepared Fe_2O_3-ZrO_2 was the first ball milled using planetary ball milled (BM4X-04, COL-INT TECH) in a zirconia container for 20 h with 300 rpm speed. Then 0.1 g Ir precursor Iridium III 2, 4 pentanedionate ($C_{15}H_{21}IrO_6$, sigma Aldrich) was dissolved in 2 ml acetone (99.5% Sigma Aldrich). Later, the solution was mixed with 1 g of milled Fe_2O_3-ZrO_2 precursor powder in an agate mortar followed by hand grinding. Finally, the obtained powders were calcined at 600 °C for 2 h in air, where IrO_2 is converted into Ir. The total IrO_2 loading is ∼4 wt% of Fe_2O_3/ZrO_2 mass.

Fe_2O_3/BZC4YYb.—BZCYYb powder was prepared by the solid-state reaction (SSR) method. $BaCO_3$ (Sigma-Aldrich, ACS Reagent, ⩾99%), CeO_2 (Acro's Organics, 99.9%), ZrO_2 (Alfa Aesar, 99.7%), Y_2O_3 (Alfa Aesar, 99.9%) and Yb_2O_3 (Sigma-Aldrich, 99.9%) were mixed accordingly with their stoichiometric with ethanol for 24 h, followed by drying in oven and calcination at 900 °C for 10 h. The powder was then ball milled by micronizing mill (Mc-Crone) for 30 min to obtain a small uniform particle size, followed by die pressing into disk and sintering at 1350 °C for 10 h. The milling, die pressing and sintering process was repeated twice to achieve the pure phase. Finally, 3.25 g Fe_2O_3 nanosized powder (99.5%, US Research Nanomaterials, Inc.) and 1.1 g BZC4YY powder were mixed using ball milling at 300 rpm speed for 20 h in ethanol (100% Sigma Aldrich) and with ZrO_2 balls using a planetary ball milling (BM4X-04, COL-INT TECH). The mixture was finally dried in oven at 80 °C and ready for use. We also measured BET surface area of the powder using Micromeritics ASAP2020 surface analyzer.

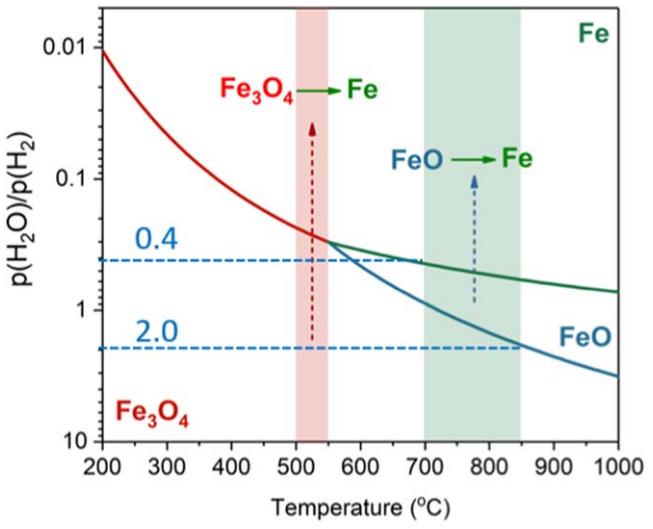

Figure 2. Baur-Glaessner's equilibrium diagram of the Fe-O-H system.[15]

Fe_2O_3/BZC4YYb-Ir.—Infiltration method was used to prepare Fe_2O_3/BZC4YYb-IrO_2. The 0.1 g of Ir precursor, iridium III 2,4-penetanedionate ($C_{15}H_{21}IrO_6$) dissolved in 2 ml of acetone was intimately mixed with 1 g of Fe_2O_3/BZC4YYb powder in an agate mortar. The powder was finally calcined at 600 °C for 2 h in air. The total loading of IrO_2 is ∼4 wt% of Fe_2O_3/BZCYYb mass.

Material characterization.—Phase compositions of the prepared composites, i.e., Ir-added Fe_2O_3/ZrO_2 and Fe_2O_3/BZC4Yb-Ir as well as post-test samples were examined by X-ray diffraction (XRD, Rigaku D/MAX-2100) at a scan rate of 3 °C min from 20° to 80°. The morphologies of the prepared materials before and after the reaction were also taken by a field emission scanning electron microscope (FESEM, Zeiss Gemini500).

Experimental setup for kinetic studies.—The reduction of the prepared composites Fe_2O_3/ZrO_2-Ir and Fe_2O_3/BZC4YYb-Ir and their respective kinetic studies were performed in a fixed bed reactor in a mixture of H_2 and H_2O. The experimental setup is shown in Fig. 1, where a quartz tube, fixed bed reactor, water bubbler, mass flow controller, switch valve, and mass spectrometer (MS, Pfeiffer Omni star 100) connected to the reactor tube outlet are depicted.

For a typical run, roughly 100 mg of the above composites are loaded on a lump of quartz wool and placed inside a quartz glass tube. The temperature is then raised to 400 °C under Ar gas at 200 cm^3 min^1. At a target temperature (500–575 °C), Ar gas is then switched to a mixture of 10% H_2 and Ar to reduce the initial Fe_2O_3 into iron. The completion of the reduction process is confirmed by the leveling off of H_2 concentration at 10% as measured by MS. After the initial full reduction, the gas is switched to a mixture of H_2-H_2O-Ar with a controlled H_2/H_2O ratio to form the desired Fe_3O_4 for reduction kinetics study. The H_2O/H_2 is set to 2 in this study according to the Fe-O-H phase diagram to form the Fe_3O_4 phase.[15] To do so, a fixed flow rate of H_2 is mixed with a room-temperature moistened (3%H_2O) Ar stream flowed at 100 sccm. We have also studied the effect of H_2 concentration on the reduction kinetics. The H_2 concentration was varied in 5%, 10%, and 20% H_2-Ar with a fixed total flow of 100 sccm. During the experiment, the effluent is constantly analyzed by an online MS for H_2O and H_2 concentrations.

Results and Discussion

Confirmation of the starting Fe_3O_4 for H_2 reduction.—Figure 2 of the thermodynamic Fe-H-O phase diagram provides the

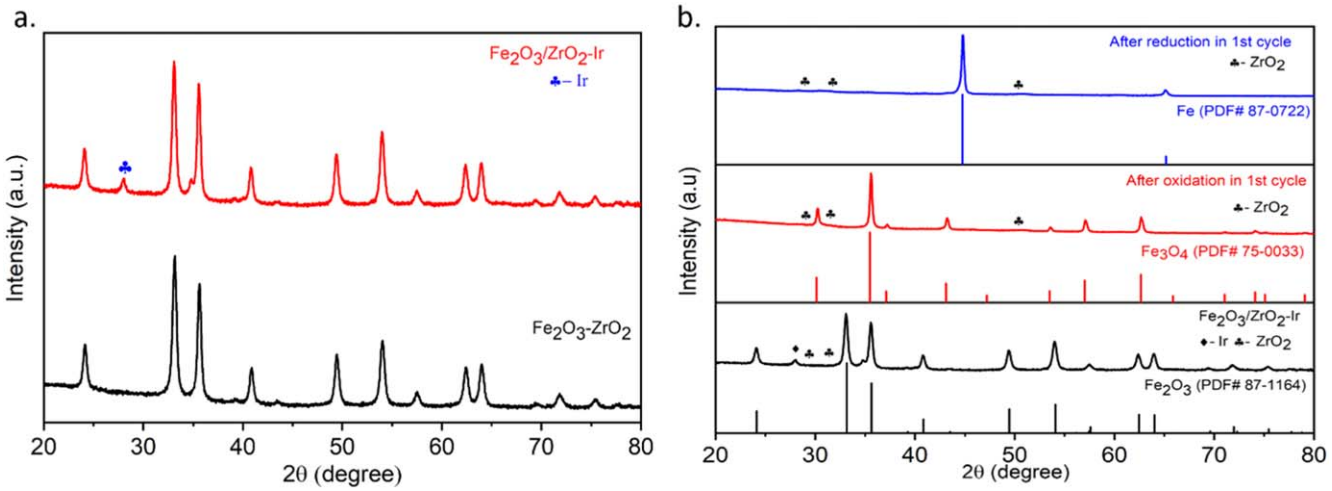

Figure 3. (a) XRD patterns of the baseline Fe_2O_3/ZrO_2 and Ir-added Fe_2O_3/ZrO_2, (b) XRD patterns of Ir-added Fe_2O_3/ZrO_2 before and after the 1st redox cycle at 500 °C.

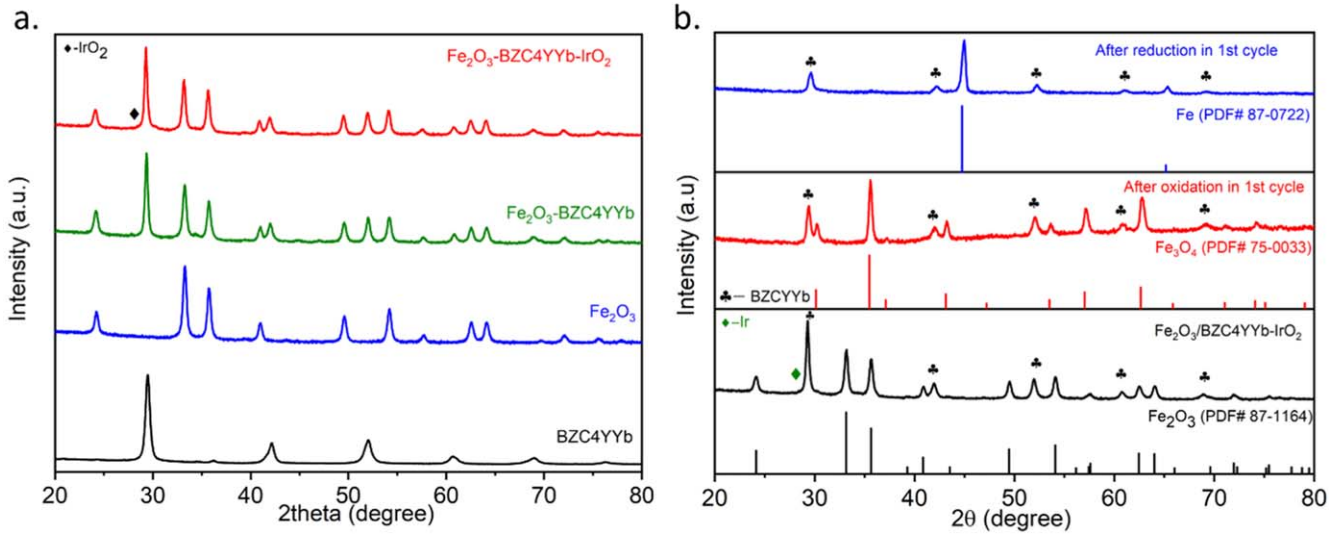

Figure 4. (a) XRD patterns of the baseline Fe_2O_3/BZC4YYb and Ir-added Fe_2O_3/BZC4YYb; (b) XRD patterns of Ir-added Fe_2O_3/BZC4YYb before and after the 1st redox cycle at 500 °C.

theoretical basis for stable Fe_3O_4 phase.[15] Within 500–575 °C, a $pH_2O/pH_2 = 2$ is a sufficient gas condition to form stable Fe_3O_4. To experimentally achieve this gas condition, we fixed H_2O content to 3% by passing 100 sccm argon through a room temperature bubbler and adding 1.5 sccm H_2 to the stream. We have experimentally confirmed the formation of Fe_3O_4 using this method by XRD and Raman spectroscopy.[15]

Phase compositions of Fe oxides before and after reduction.— The starting phase compositions of Ir-added Fe_2O_3-ZrO_2 and Fe_2O_3/BZC4YYb are shown in Fig. 3a of XRD patterns. The Fe_2O_3/ZrO_2 system shows distinct peaks at 24, 33.2, 35.6, 40.8, 49.5, 54.1,62.4, 63.98°, which can be attributed to the planes (012), (104), (110), (024), (116), (214), (300) of Fe_2O_3 (PDF♯ 84–0308). These sharp and well-defined peaks indicate the high crystallinity and purity of the sample synthesized through co-precipitation. After introducing Ir (initially IrO_2) to the composite, a broad peak appears at 28.1°, corresponding to the (110) plane of Ir. However, the peaks of Ir exhibit low intensity and broadening, indicating lower crystallinity. Figure 3b shows the phase composition after the first redox cycle at 500 °C. Despite the redox process, all XRD peaks of ZrO_2 remain unchanged, indicating the chemical stability of ZrO_2. The

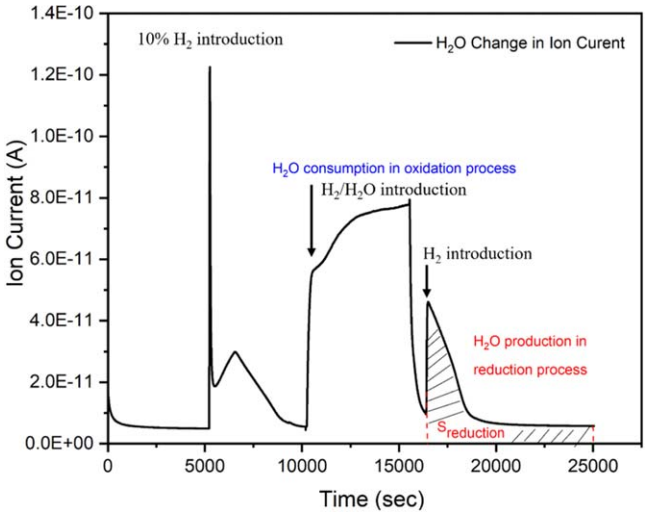

Figure 5. An exemplary profile of the ionic current related to the steam concentration measured by MS.

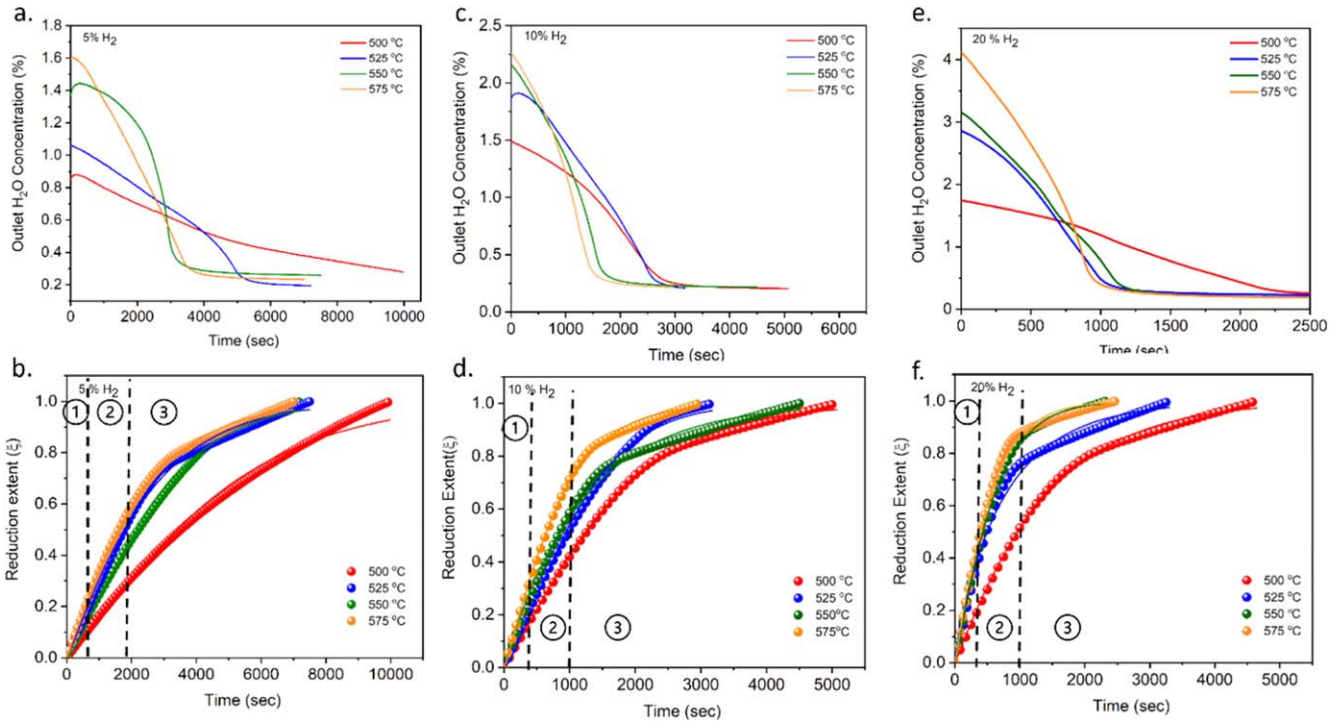

Figure 6. Profiles of outlet steam concentration and reduction extent (dot) vs time during reduction and JMA reduction model fitting curves (line) of Fe_3O_4/ZrO_2_Ir. Temperature: 500 to 575 °C. 5% H_2 (a) and (b), 10% H_2 (c) and (d) and 20% H_2 (e) and (f).

Table I. Reduction kinetic data for Fe_3O_4/ZrO_2-Ir and Fe_3O_4/BZC4YYb-Ir systems.

Reduction kinetics data for Fe_3O_4/ZrO_2-Ir

	5% H_2				10% H_2				20% H_2			
T (°C)	500	525	550	575	500	525	550	575	500	525	550	575
k*10^{-4} (s^{-1})	0.29	0.35	0.62	0.24	2.13	2.24	5.53	5.00	5.02	9.14	7.03	10.9
n		1.08				1.08				1.08		
E_a ($kJmol^{-1}$)		149.8				75.3				45.0		

Reduction kinetics data for Fe_3O_4/BZC4YYb-Ir

	5% H_2				10% H_2				20% H_2			
T (°C)	500	525	550	575	500	525	550	575	500	525	550	575
k*10^{-4} (s^{-1})	0.51	0.52	2.81	1.94	1.36	5.27	16.10	7.22	10.20	21.3	53.1	41.0
n		1.01				1.01				1.01		
E_a ($kJmol^{-1}$)		115.6				122.0				103.0		

presence of Fe and Fe_2O_3 results in the weakening of the peak at 28.2° likely due to the high crystallinity and high content of Fe-related phases, suggesting that the ZrO_2 phase maintains its integrity and stability. Note that Fe_3O_4 after oxidation is observed in Fig. 3b.

The phase purity of the prepared BZC4YYb is confirmed by the XRD pattern in Fig. 4a. When BZC4YYb is mixed with Fe_2O_3, no additional peaks are observed. This indicates that the original phase of BZC4YYb has been preserved after mixing. After introducing Ir, a very small peak appears at 28.0° corresponding to the (110) plane of Ir, like the early case. However, the Ir peak has low intensity and crystallinity. Figure 4b shows the phase compositions of the materials after the first redox cycle at 500 °C; all XRD patterns of BZC4YYb remain unchanged, suggesting good chemical stability of BZC4YYb. After the oxidation cycle, we observe Fe_3O_4 peaks, and after reduction, it is converted to metallic Fe.

Reduction kinetics modeled by Johnson-Mehl-Avrami theory.—The Johnson-Mehl-Avrami, *aka.* JMA, theory describes isothermal reduction kinetics with solid-state phase transformation consideration.[19–21] The JMA theory is commonly applied to simulate solid state phase transformations, such as crystallization and precipitation.[22] This transformation involves the formation and growth of a new solid phase within a parent phase. A new phase is a germ nucleated and distributed throughout the solid, followed by grain growth of an old phase until transformation is completed.[19] The reduction process of FeO_x by H_2 normally involves a sequence of nucleation and growth steps.[15] The measured isothermal reduction fraction (ξ) vs time is expressed by

$$\xi(t) = \frac{\int_0^t (I_{H2Oprod})dt}{S_{red}} \quad [1]$$

Here, $I_{H2O\ prod}$ is time-dependent ion current of MS proportional to H_2O concentration; S_{red} is the peak area of full reduction process as shown in Fig. 5.

The JMA model correlates $\xi(t)$ with the kinetic rate constant k(T) by.[23–26]

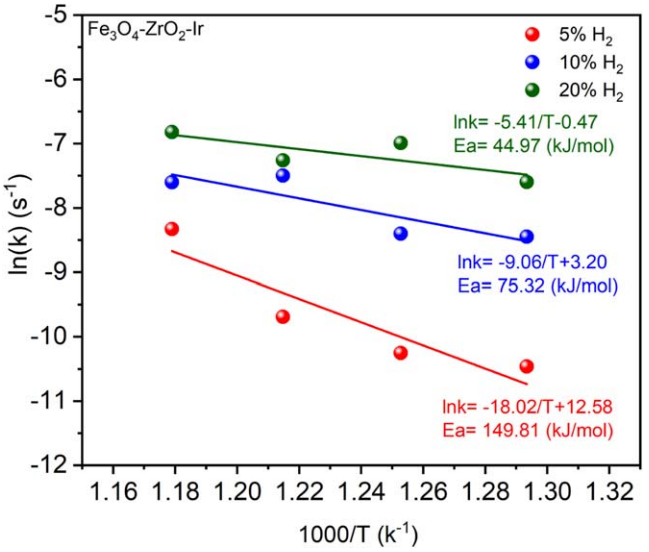

Figure 7. Arrhenius plot of rate constant of Fe_3O_4-to-Fe reduction extracted from JMA model.

$$\xi(t) = 1 - \exp[-k(T)t^n] \quad [2]$$

where

$$k(T) = A_* \exp\left(-\frac{E_a}{RT}\right).$$

A logarithmic rearrangement of Eq. 2 leads to the Sharp-Hancock equation for studying the order of solid-state reaction.[27]

$$\ln[-\ln(1-\xi)] = n\ln(t) + \ln(k) \quad [3]$$

where n is Avrami exponent, which depends on the nucleation and crystal growth of a phase boundary surface.[27] Generally, $n = \lambda + \beta$, where λ is the dimensionality of growth, $\lambda = 1$, 2 or 3 and β depends on the nucleation process to the overall kinetics ($0 < \beta < 1$, 0 represents instantaneous nucleation and 1 means a very slow nucleation rate).[7] The valve of n = 1–2 signifies 1D growth, n = 2–3 for 2D growth and n = 3–4 for 3D growth for each process at a temperature.[19]

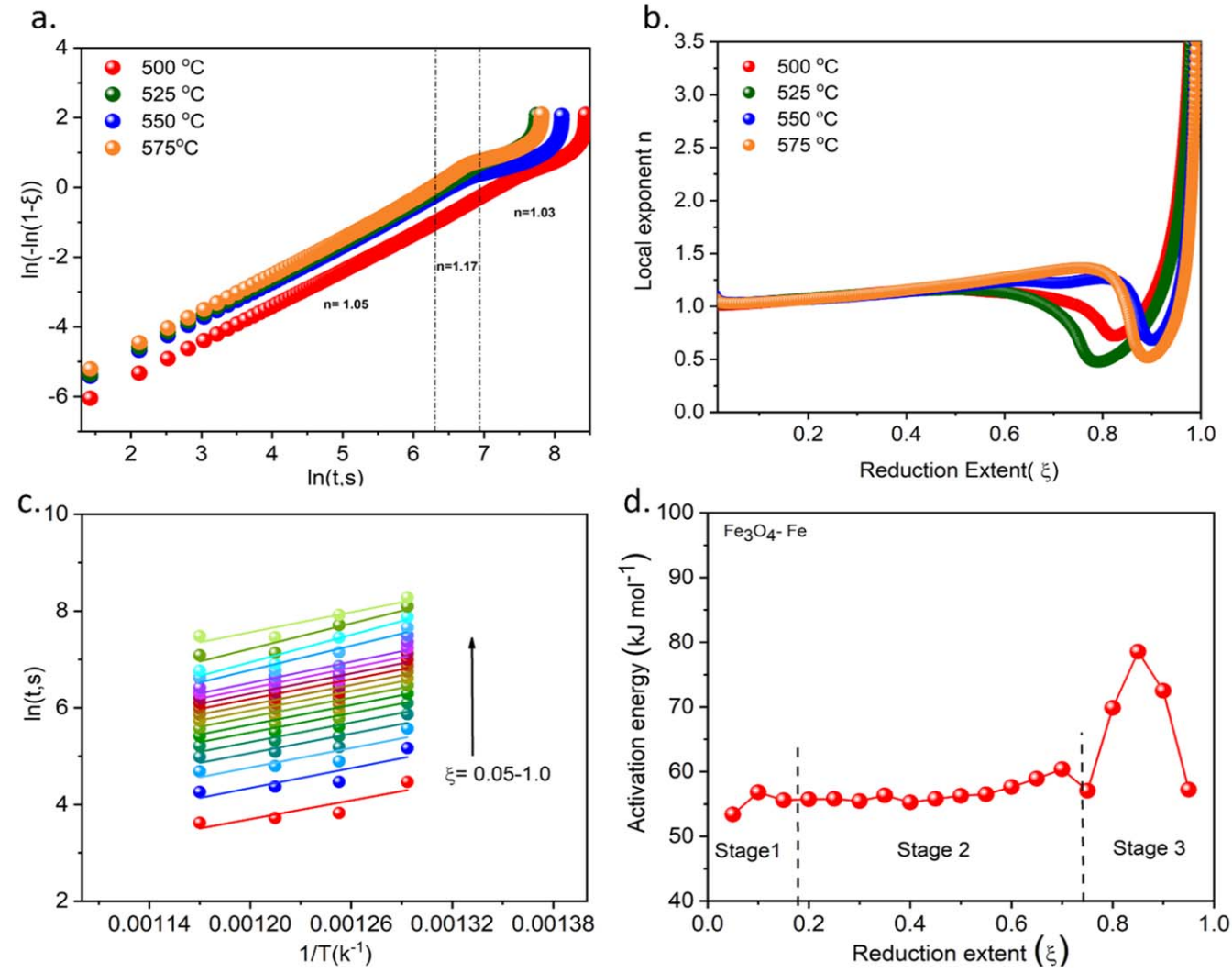

Figure 8. Kinetic data for Fe_3O_4/ZrO_2-Ir: (a) Sharp-Hancock plots of $\ln(-\ln(1-\xi))$ vs ln (t) at 500 to 575 °C in 20% H_2. (b) local exponent n values vs reduction extent at 500 to 575 °C in 20% H_2. (c) ln(t) vs1/T with different reduction extents at 500 to 575 °C in 20% H_2. (d) Activation energy as a function of the reduction extent for the Fe_3O_4 to Fe conversion.

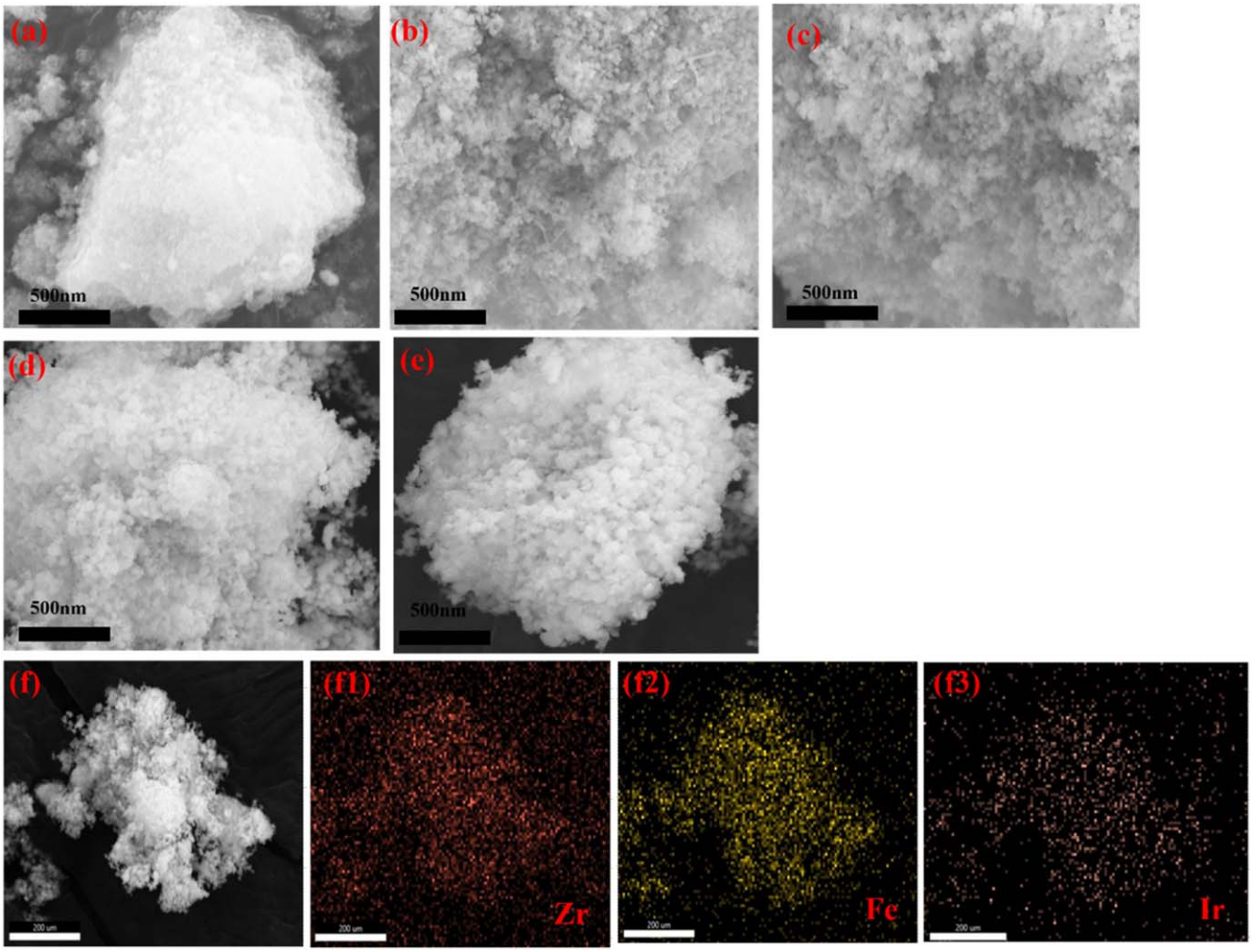

Figure 9. SEM images of active materials of (a) fresh Ir-added Fe_2O_3/ZrO_2 and after reduction in 20% H_2 at (b) 500, (c) 525, (d) 550 and (e) 575 °C. Area of elemental mapping of reduced sample at 550 °C for (f1) Zr, (f2) Fe and (f3) Ir.

The local n (ξ) can be calculated by differentiating Eq. 3.

$$n(\xi) = \frac{\partial \ln(-\ln(1-\xi))}{\partial \ln(t)} \quad [4]$$

For the iron oxide reduction process, the reaction rates can also be expressed as

$$\frac{d\xi}{dt} = k(T)_* f(\xi) \quad [5]$$

where f(ξ) is an integral mathematical function depending on kinetic model. For the reduction kinetics under isothermal conditions, it can be integrated to yield the following expression:

$$g(\xi) = \int_0^{\xi} \frac{d\xi}{f(\xi)} = k_* t = A_* \exp\left(\frac{E_a}{RT}\right) t \quad [6]$$

where g(ξ) is an integral mathematical function related to the mechanism of reduction reaction. Using logarithmic form and rearrangement of Eq. 6, we get

$$\ln(t) = (-\ln(A) + \ln(g(\xi)) + \frac{Ea}{RT} \quad [7]$$

where t is the reaction time corresponding to reduction extent ξ. By plotting ln(t) vs 1/T, activation energy E_a can be obtained as a function of reduction extent.

Reduction kinetics and morphology of Fe_3O_4/ZrO_2-Ir.—The reduction kinetics of Fe_3O_4/ZrO_2-Ir to Fe/ZrO_2-Ir was obtained by the measured H_2O concentration with MS. The change in outlet H_2O concentration and reduction extent ξ vs t during the reduction process at 500 to 575 °C under different inlet H_2 concentrations are shown in Figs. 6a, 6c, and 6e, while the JMA model-processed data are shown in Figs. 6b, 6d and 6f.

It is obvious that the reduction kinetics is significantly affected by both temperature and H_2 concentration. The production of H_2O is faster in the early stages than the later stages of the process as expected. All isotherm plots of ξ(t) exhibit a sigmoid shape and can be generally divided into three different regions: ① incubation period ($0 < \xi < 0.1$), ② acceleration regions ($0.1 < \xi < 0.65$) and ③ deceleration region ($0.65 < \xi < 1.0$). As temperature increases, ξ shows shorter incubation period, indicating nucleation events dominate this period. The acceleration region is associated with the development of a new phase, while the deceleration region corresponds to the termination growth due to the coalescence of Fe, which affects diffusion.[15] The fitting provides values for kinetic rate constant (k) and exponent(n), which is summarized in Table I. The average Avrami exponent (n) is 1.08, indicating that the reduction process follows 1D growth ($\lambda = 1$) with small nucleation contribution.[15]

With Eq. 1, the obtained kinetic rate constants are further plotted in Fig. 7 in Arrhenius format, yielding activation energy of 149.81, 75.32 and 44.97 kJ mol^{-1} for 5, 10 and 20% H_2 respectively, suggesting a higher energy barrier for lower concentration of hydrogen.

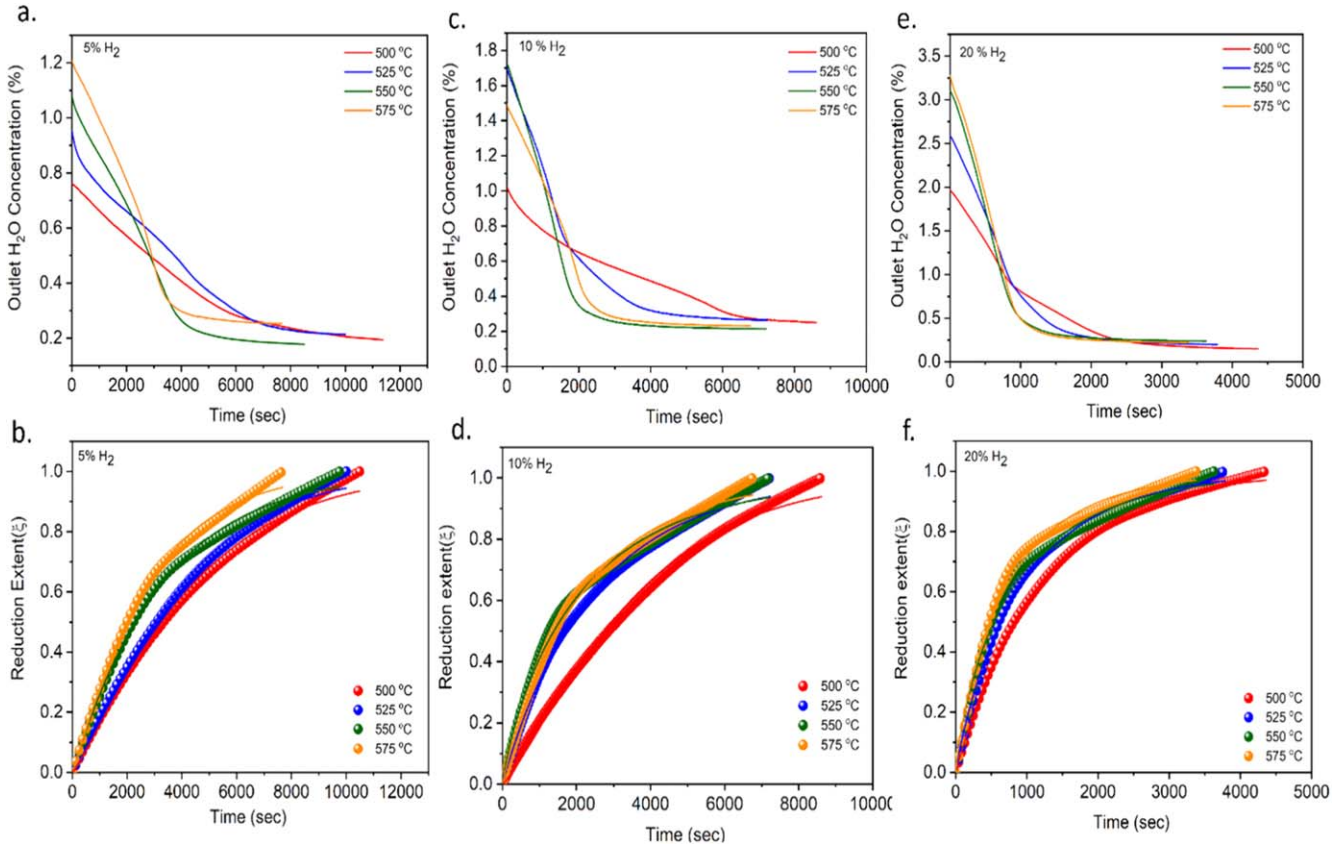

Figure 10. Profiles of outlet water concentration during reduction process and corresponding reduction extent (dot) of Fe_3O_4 vs time and JMA reduction model fitting curves (line) from 500 to 575 °C in 5% H_2 (a) and (b), 10% H_2 (c) and (d) and 20% H_2 (e) and (f) of Fe_3O_4/BZC4YYb-Ir.

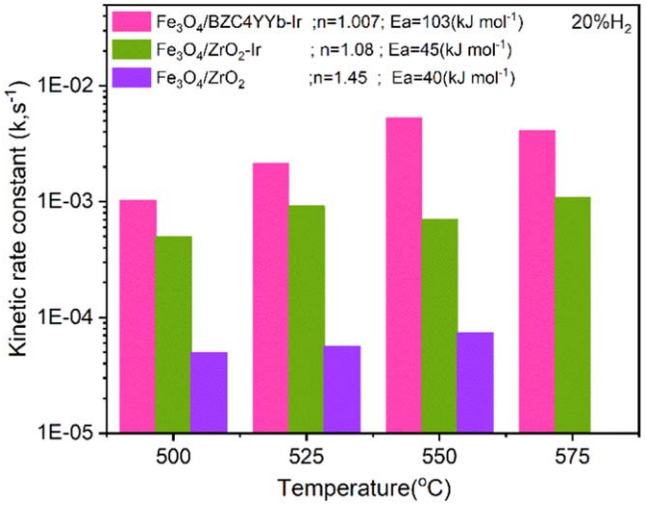

Figure 11. Comparison of reduction kinetics rate constants among three Fe-based energy storage systems in 20% H_2.

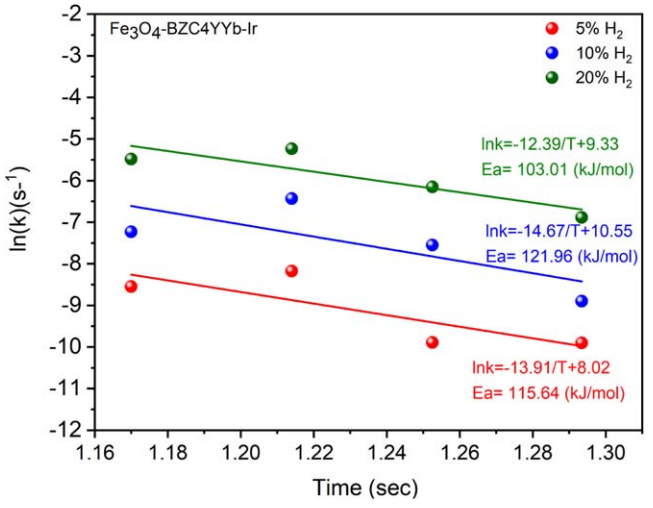

Figure 12. Arrhenius plot of rate constant of reduction in Fe_3O_4/BZCYYb-Ir system.

To examine the dependence of n on reduction extent ξ, we used Sharp and Hancock equation (Eq. 3). Figure 8a shows an exemplary plot of ln (-ln(1− ξ)) vs ln(t) at 500 to 575 °C in 20% H_2-Ar. Three distinct stages are identified for the entire conversion process, each characterized by a unique n. When the reduction extent approaches 1, the Avrami exponent n approaches to infinity (($\xi \neq 1$ is the boundary condition for Eq. 3). The variation of local exponent n with reduction extent ξ signifies the different dominant mechanisms in each stage of the reaction.[15]

A further analysis of the Avrami exponent (n) reveals interesting behavior during the different stages of the reduction. Initially, as the reduction begins, Fig. 8b shows that n slowly increases and reaches a maximum value. This indicates a 1D growth process with a decreasing nucleation rate. Towards the end of the reaction, n tends to fall below 1, suggesting a slow diffusion-controlled process, which can be attributed to the partial sintering of Fe particles affecting diffusion. To gain further insight into the mechanism, Eq. 7 is utilized to plot ln(t) against 1/T in Fig. 8c at reduction extent (ξ) from 0.05 to full reduction extent (ξ = 1) in 20% H_2. From the

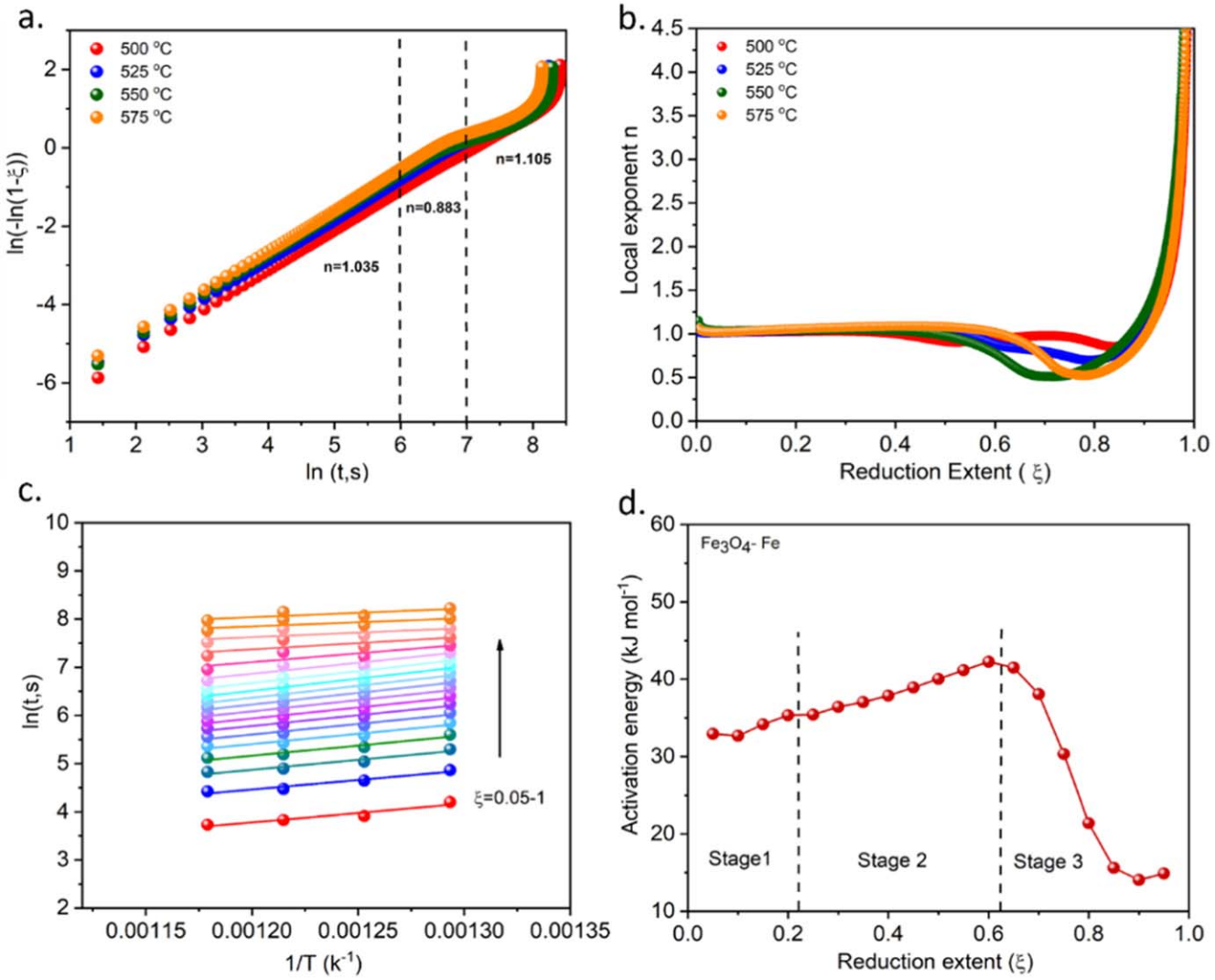

Figure 13. Kinetic data for Fe_3O_4/BZC4YYb-Ir: (a) Sharp-Hancock plots of ln(−ln(1- ξ)) vsln (t) based on the data at 500 to 575 °C in 20% H_2. (b) local exponent n values vs reduction extent at 500 to 575 °C in 10% H_2. (c) ln(t) vs 1/T with different reduction extents at 500 to 575 °C in 20% H_2. (d) Activation energy as a function of the reduction extent for the Fe_3O_4 to Fe conversion.

activation energy (E_a) calculated from the slope of each line, Fig. 8d indicates that E_a initially increases from 53.39 to 55.6 kJ mol^{-1} within the range of $0.05 < \xi < 0.15$, followed by a slow increase to 60.38 kJ mol^{-1} within $0.15 < \xi < 0.7$ and appreciable increase to 78.54 kJ mol^{-1} for $0.75 < \xi < 0.85$, and finally decreases to 57.22 kJ mol^{-1} towards the end of the reduction process. This variation in E_a suggests changes in the growth and nucleation mechanism during the reduction process.

Particle sintering of the active materials can impact the kinetics and mechanisms. To verify if there is a significant change in particle morphology, Fig. 9 compares SEM images of the as prepared and tested Fe_2O_3/ZrO_2-Ir. The fresh sample in Fig. 9a consists of agglomerates of nanoparticles. After reduction in 20% H_2 at 500 to 575 °C, Figs. 9b–9d shows some minor agglomeration from 500 to 550 °C and worst agglomeration at 575 °C, which could be evidence for slowed kinetics at the final stage of reduction. The elemental mapping of the reduced sample is shown in Figs. 9e–9f with uniform distribution of Fe, Zr, and Ir.

Reduction Kinetics of Fe_3O_4/BZC4YYb-Ir.—The reduction kinetics of Fe_3O_4/BZC4YYb-Ir to Fe/BZC4YYb-Ir was determined by a similar method to the Fe_3O_4/ZrO_2-Ir system. The raw data of H_2O concentration in the effluent and the corresponding reduction extent of Fe_3O_4 with time are shown in Fig. 10. The kinetic rate constant (k), the exponent(n) and the activation energy (E_a) obtained are summarized in Table I. The k-value of Fe_3O_4/BZC4YYb-Ir system appears to be higher than the Fe_3O_4/ZrO_2-Ir system, especially at high H_2 concentration. Figure 11 compares the logarithmic value of the kinetic rate constant of three Fe-based materials within a temperature range of 500–575 °C in 20% H_2; the results indicates that the kinetic rate constant of Fe_3O_4/ZrO_2-Ir is one order magnitude higher than the baseline.[28] By replacing supporting oxide ZrO_2 with BZCYYb, the kinetic rate constant again is one order magnitude higher. This shows that both Ir catalyst and proton containing BZCYYb support help boost the reduction kinetics. We stress here that the ability of BZCYYb to boost reduction kinetics is not due to higher surface area but its proton containing property. In fact, the measured BET of BZCYYb is 34 m^2 g^{-1}, close to 30 m^2 g^{-1} of the baseline.

The average value of n is 1.01, indicating that the phase transition follows 1D growth ($\lambda = 1$) with very small nucleation contribution. The activation energy obtained from the Arrhenius plot of k shown in Fig. 12 are 115.64, 121.96, and 103.01 kJ mol^{-1} for 5, 10 and 20% H_2 respectively, which are much higher than Fe_3O_4/ZrO_2-Ir system.

Similarly, ln(-ln(1- ξ)) vs ln(t) are plotted in Fig. 13a for 500 to 575 °C in 20% H_2-Ar. The same trend is observed as in the Fe_3O_4/ZrO_2-Ir system. At the beginning of the reduction, the average

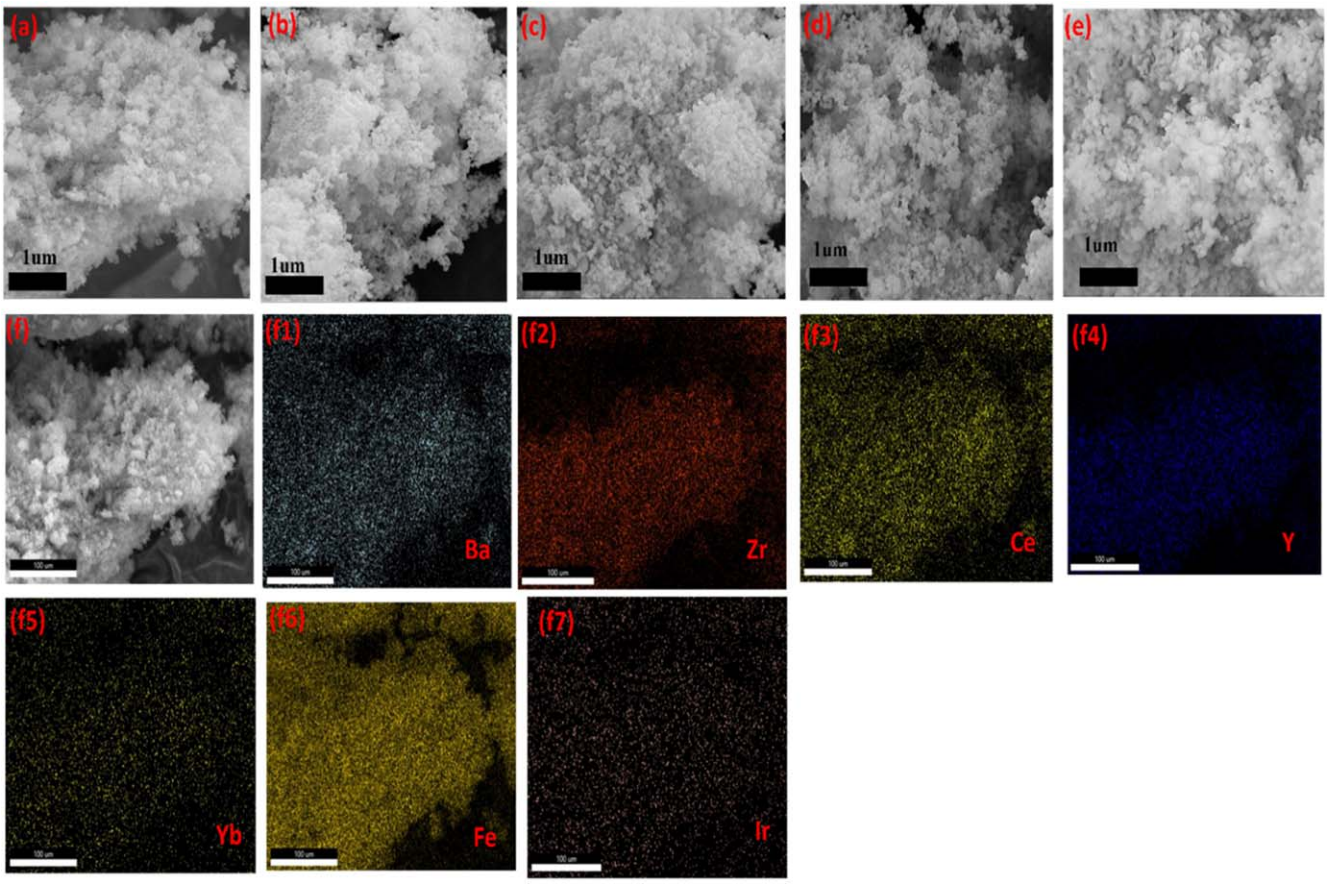

Figure 14. SEM images of powders of (a) fresh Fe_2O_3/BZC4YYb-Ir and after reduction in 20% H_2 at (b) 500, (c) 525, (d) 550 and (e) 575 °C. Elemental mapping of reduced sample at 550 °C for (f1) Ba, (f2) Zr, (f3) Ce, (f4) Y, (f5) Yb, (f6) Fe and (f3) Ir.

n value is 1.03, at the intermediate stage n decreases to 0.88 and finally increases 1.10 to at the final stage. The variation of local exponent n with reduction extent ξ is shown in Fig. 13b; it signifies the different dominant mechanism in each stage of the reaction.[15] The explanations given for the Fe_3O_4/ZrO_2-Ir system previously are applicable to the Fe_3O_4/BZCYYb-Ir system. The plot of ln(t) vs 1/T using Eq. 7 at ξ varying from 0.05 to 1 from 500 to 575 °C in 20% H_2 atmosphere is shown in Fig. 13c, from which the activation energy (E_a) is obtained and plotted in Fig. 13d. The results indicate that E_a initially increases with ξ from 32.93 to 35.32 kJ mol^{-1} within $0.05 < \xi < 0.2$, followed by a gradual increase to 42.259 kJ mol^{-1} within $0.2 < \xi < 0.6$. Finally, it decreases to 14.86 kJ mol^{-1} towards the end of the reduction process. This variation in E_a suggests changes in growth and nucleation mechanisms during the reduction process. Note that E_a derived from isothermal ξ is much smaller for Fe_3O_4/BZCYYb-Ir than Fe_3O_4/ZrO_2-Ir, implying that it is easier for the former than the latter to be reduced isothermally. The ability of BZCYYb to retain water thus proton has been previously postulated as the mechanism for the boosted reduction kinetics.[18]

The morphologies of Fe_3O_4/BZC4YYb/Ir before and after reduction are shown in Fig. 14 of SEM image. After reduction at 500 to 575 °C, Figs. 14b–14d show that particles are slightly agglomerated with temperature as expected. Agglomeration observed is like the case of Fe_3O_4/ZrO_2-Ir (see Fig. 9). The elemental mapping in Figs. 14f1–14f7 of the reduced sample shows the uniform distribution of Ba, Zr, Ce, Y, Yb, Fe and Ir.

Conclusions

The kinetics of Fe_3O_4 reduction by H_2 with Ir as a catalyst and ZrO_2 and BZCYYb as supporting oxides was studied as a function of H_2 concentration and temperature. The desired starting Fe_3O_4 was obtained in situ by controlling the partial pressure ratio of H_2O and H_2 to 2. The degree of Fe_3O_4 reduction was obtained by an on-line mass spectrometer. It was found that the reduction kinetics follows Johnson-Mehl-Avrami (JMA) phase transformation model, showing three stages during the reduction. From the kinetic analysis, Fe_3O_4 reduction degree (ξ) was shown to obey the 1D growth with decrease in the nucleation rate. The activation energies of both ZrO_2 and BZCYYb based materials experience a "peaking" behavior with reduction extent. In addition, toward the end of reduction period, coarsening of Fe particles could affect the kinetics, resulting in higher E_a. By adding Ir as a catalyst and using proton-containing supporting oxide in the baseline energy storage unit, a significantly boosted kinetics has been observed. Since the activation energy (E_a) of Fe_2O_3/ZrO_2-Ir and Fe_2O_3/BZCYYb-Ir is higher than the baseline, the high pre-exponential factor (A) related to the number of active sites must be the reason for the boosted kinetics.

Acknowledgments

We would like to thank the National Science Foundation for the financial support under award no. 1801284.

ORCID

Kevin Huang https://orcid.org/0000-0002-1232-4593

References

1. P. Denholm and M. Hand, *Energy Policy*, **39**, 1817 (2011).
2. W. A. Braff, J. M. Mueller, and J. E. Trancik, *Nat. Clim. Change*, **6**, 964 (2016).
3. M. R. Shaner, S. J. Davis, N. S. Lewis, and K. Caldeira, *Energy Environ. Sci.*, **11**, 914 (2018).
4. O. J. Guerra, J. Zhang, J. Eichman, P. Denholm, J. Kurtz, and B.-M. Hodge, *Energy Environ. Sci.*, **13**, 1909 (2020).

5. J. A. Dowling, K. Z. Rinaldi, T. H. Ruggles, S. J. Davis, M. Yuan, F. Tong, N. S. Lewis, and K. Caldeira, *Joule*, **4**, 1907 (2020).
6. C. A. Hunter, M. M. Penev, E. P. Reznicek, J. Eichman, N. Rustagi, and S. F. Baldwin, *Joule*, **5**, 2077 (2021).
7. P. Albertus, J. S. Manser, and S. Litzelman, *Joule*, **4**, 21 (2020).
8. R. E. Ciez and D. Steingart, *Joule*, **4**, 597 (2020).
9. C. Zhang and K. Huang, *ACS Energy Lett.*, **1**, 1206 (2016).
10. X. Zhao, X. Li, Y. Gong, N. Xu, and K. Huang, *RSC Adv.*, **4**, 22621 (2014).
11. X. Zhao, X. Li, Y. Gong, and K. Huang, *Chem. Commun.*, **50**, 623 (2004).
12. X. Zhao, Y. Gong, X. Li, N. Xu, and K. Huang, *J. Electrochem. Soc.*, **160**, A1241 (2013).
13. X. Jin, X. Zhao, and K. Huang, *J. Power Sources*, **280**, 195 (2015).
14. Q. Tang, Y. Zhang, N. Xu, X. Lei, and K. Huang, *Energy Environ. Sci.*, **15**, 4659 (2022).
15. Q. Tang and K. Huang, *Chem. Eng. J.*, **434**, 134771 (2022).
16. Q. Tang, Y. Ma, and K. Huang, *ACS Appl. Energy Mater.*, **4**, 7091 (2021).
17. N. Xu, C. Zhang, and K. Huang, *J. Mater. Chem. A*, **6**, 20659 (2018).
18. Q. Tang, C. Morey, Y. Zhang, N. Xu, S. Sun, and Kevin Huang, *Adv. Sci.*, **9**, 2203768 (2022).
19. K. Piotrowski, K. Mondal, T. Wiltowski, P. Dydo, and G. Rizeg, *Chem. Eng. J.*, **131**, 73 (2007).
20. C. E. Seaton, J. S. Foster, and J. Velasco, *Trans. Iron Steel Inst. Jpn.*, **23**, 490 (1983).
21. S. S. Jung and J. S. Lee, *Mater. Trans.*, **50**, 2270 (2009).
22. M. C. Weinberg, D. P. Birnie, and V. A. Shneidman III, *J. Non-Cryst. Solids*, **219**, 89 (1997).
23. M. Avrami, *J. Chem. Phys.*, **7**, 1103 (1937).
24. M. Avrami, *J. Chem. Phys.*, **8**, 212 (1940).
25. M. Avrami, "Granulation." *J. Chem. Phys.*, **9**, 177 (1941).
26. B. V. Erofe'ev, *Compt. Rend. Acad. Sci. USSR*, **52**, 511 (1946).
27. E. R. Monazam, R. W. Breault, and R. Siriwardane, *Energy Fuels*, **28**, 5406 (2014).
28. C. Morey, Q. Tang, and K. Huang, *ECS Trans.*, **111**, 1771 (2023).